

RESEARCH ARTICLE

# A comprehensive study of second and third harmonic conversion efficiency, angular and temperature tolerance and long-term stability in lithium triborate crystals using a 10-J-class laser

Huzefa Aliasger<sup>1,2</sup>, Ondřej Novák<sup>1</sup>, Zbyněk Hubka<sup>1</sup>, Martin Hanuš<sup>1</sup>, Petr Navrátil<sup>1</sup>, Patricie Severová<sup>1</sup>, Ondřej Denk<sup>1,2</sup>, Jan Pilař<sup>1</sup>, Tomáš Paliesek<sup>1,2</sup>, Martin Divoký<sup>1</sup>, Ondřej Schreiber<sup>3</sup>, Michal Jelínek<sup>2</sup>, Martin Smrž<sup>1</sup>, and Tomáš Mocek<sup>1</sup>

<sup>1</sup>HiLASE Centre, Institute of Physics of the Czech Academy of Sciences, Dolní Břežany, Czech Republic

<sup>2</sup>Department of Laser Physics and Photonics, Faculty of Nuclear Sciences and Physical Engineering, Czech Technical University in Prague, Praha 1, Czech Republic

<sup>3</sup>Narran s.r.o., Bayerova 802/33, Brno, Czech Republic

(Received 19 May 2025; revised 25 July 2025; accepted 28 August 2025)

## Abstract

We present a study of second harmonic generation (SHG) and third harmonic generation (THG) in lithium triborate (LBO) crystals using a high-energy, 10-J-class, 10 Hz ytterbium-doped yttrium aluminum garnet laser system. We achieved high conversion efficiencies of 75% for SHG and 56% for THG for Gaussian-like temporal pulse shapes and top-hat-like beam profiles. The angular and temperature dependence of the LBO crystals was measured and validated through numerical simulations. The SHG process exhibited an angular acceptance bandwidth of 1.33 mrad and a temperature acceptance bandwidth of 2.61 K, while the THG process showed 1.19 mrad and 1.35 K, respectively. In addition, long-term stability measurements revealed root mean square energy stabilities of 1.3% for SHG and 1.24% for THG. These results showcase the reliability of LBO crystals for high-energy, high-average-power harmonic generation. The developed system offers automated switching between harmonics provided at the system output. The system can be easily adapted to neodymium-doped yttrium aluminum garnet based pump lasers as well.

**Keywords:** angular acceptance bandwidth; frequency conversion; high average power; high energy; lithium triborate; long-term stability; temperature acceptance bandwidth

## 1. Introduction

The interaction of matter at high-energy, high-power lasers has paved a way to explore opportunities in real-world applications such as laser particle acceleration<sup>[1]</sup>, medical treatments<sup>[2]</sup>, precision micromachining<sup>[3]</sup>, laser shock peening<sup>[4,5]</sup> and laser-driven fusion<sup>[6–8]</sup>. Ytterbium-doped nanosecond (ns) solid-state lasers are of significant interest due to their suitability for high-energy, high-power and high-repetition-rate applications<sup>[9]</sup>. This suitability arises from their millisecond-scale fluorescence lifetime, superior thermal conductivity (attributed to their yttrium aluminum garnet (YAG) host) and compatibility with diode laser pump-

ing<sup>[10,11]</sup>. The high-energy pulses from ytterbium-doped yttrium aluminum garnet (Yb:YAG), which are around 1030 nm, can be used as a pre-amplifier in a chirped pulse amplification (CPA) system<sup>[12]</sup>. However, they are not suitable for pumping optical parametric chirped pulse amplification (OPCPA) systems or Ti:sapphire lasers, which generate femtosecond pulses at 800 nm and require a high-energy pump source around 500 nm<sup>[13–15]</sup>. Therefore, frequency conversion techniques such as second harmonic generation (SHG) must be used to address this wavelength mismatch, thereby enhancing the utility of high-energy and high-power lasers. Furthermore, high-energy pulses at even shorter ultraviolet (UV) wavelengths are essential for laser annealing of semiconductors<sup>[16]</sup>. These UV pulses can be generated through third harmonic generation (THG) of a 1  $\mu$ m laser.

Correspondence to: H. Aliasger, HiLASE Centre, Institute of Physics of the Czech Academy of Sciences, Za Radnicí 828, 25241 Dolní Břežany, Czech Republic. Email: [huzefa.bhanpurwala@hilase.cz](mailto:huzefa.bhanpurwala@hilase.cz)

© The Author(s), 2025. Published by Cambridge University Press in association with Chinese Laser Press. This is an Open Access article, distributed under the terms of the Creative Commons Attribution licence (<https://creativecommons.org/licenses/by/4.0/>), which permits unrestricted re-use, distribution and reproduction, provided the original article is properly cited.

In the past, several groups around the world have succeeded to convert the frequency of high-energy pulses at around 1  $\mu\text{m}$ , successfully generating high-energy pulses in the green and UV spectra. Phillips *et al.*<sup>[17]</sup> reported SHG conversion efficiency of 82% using lithium triborate (LBO) crystal, achieving 5.6 J at a repetition rate of 10 Hz from 1030 nm. Also, Philips *et al.*<sup>[18]</sup> demonstrated SHG with a conversion efficiency of 66%, achieving 59.7 J at 515 nm with a repetition rate of 10 Hz, and THG at conversion efficiency of 68%, achieving 65 J at 343 nm at a repetition rate of 1 Hz. Sekine *et al.*<sup>[19]</sup> achieved 12.5 J at 527 nm using cesium lithium borate (CLBO) crystal, with a conversion efficiency of 71.5% at a repetition rate of 0.6 Hz. Chi *et al.*<sup>[20]</sup> reported 0.94 J laser pulses at 515 nm with 2 ns duration and 1 kHz repetition rate, achieving 78% efficiency using LBO crystal. Divoky *et al.*<sup>[21]</sup> reported SHG achieving 95 J at 515 nm and 10 Hz, marking the highest energy ever achieved in the green spectrum at this repetition rate. Pilar *et al.*<sup>[22]</sup> reported THG achieving 50 J at 343 nm with a repetition rate of 10 Hz, marking the highest energy ever achieved at this repetition rate.

In this paper, we present the results of SHG and THG in LBO crystals using the output beam from a 10 J Bivoj amplifier operating at a repetition rate of 10 Hz. Unlike the top-hat temporal profile employed by Phillips *et al.*<sup>[17]</sup>, we utilized Gaussian-like pulses while maintaining a spatial top-hat beam profile, achieving high conversion efficiencies of 75% for SHG and 56% for THG. We conducted detailed measurements of the angular and temperature dependencies of the LBO crystals, which were further corroborated by numerical simulations. Furthermore, we characterized the

long-term energy stability of the SHG as well as THG process in the LBO crystals.

## 2. Experimental setup

A schematic of the experimental setup is shown in Figure 1. The driving laser beam stems from the 10 J amplifier of the Bivoj laser system<sup>[11,23]</sup>. The Bivoj laser is a cryogenically cooled Yb:YAG multipass amplifier system that delivers a beam at 1030 nm and operates at a repetition rate of 10 Hz. The temporal pulse profile was adjusted to provide 8 ns Gaussian-like pulses. We decided to use Gaussian-like pulses for this study because they represent the typical pulse shape of ns lasers. Achieving a top-hat temporal profile requires a specialized front-end configuration, which is not commonly available in standard commercial laser systems and often involves added complexity and cost. The square-shaped, top-hat-like beam from the Bivoj amplifier is relayed to the optical table in a different part of the laboratory with the help of the laser beam distribution system (LBDS), which contains several imaging telescopes.

On the optical table, the p-polarized fundamental laser beam is first directed towards the harmonic generation system using mirrors M1, M2 and M3. These mirrors enable alignment of the input beam. The leakage of the laser beam through mirror M1 is utilized to monitor the input fundamental energy using energy meter EM1 (Ophir PE50-C), while the leakage from mirror M3 is used to monitor the near-field profile of the input fundamental beam via camera C1 after its demagnification by a telescope. A polarizing beam

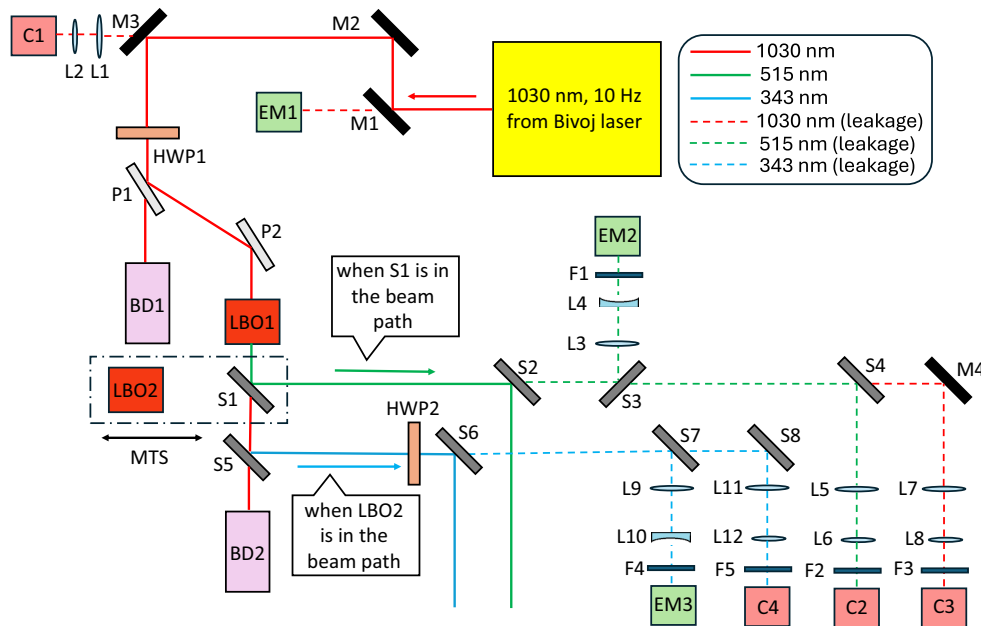


**Figure 1.** Experimental setup. M, mirrors; HWP, half-wave plates; P, polarizers; S, harmonic separators (dichroic mirrors); L, lenses; C, cameras; EM, energy meters; BD, beam dumps; F, filters; MTS, motorized translation stage.

splitter (PBS) cube was also placed before EM1 and C1 to ensure that only the p-polarized component of the beam was transmitted onto the diagnostics, but it is not shown in [Figure 1](#) for the sake of simplicity. The attenuator at the input of the system consists of a half-wave plate HWP1 mounted on a motorized rotation stage and two thin-film Brewster polarizers P1 and P2. The attenuator is used to control the energy of the laser pulses entering the nonlinear crystals without affecting their spatial or temporal shape. The s-polarized part of the beam is reflected by the polarizers and guided into the nonlinear crystals for harmonic generation. The p-polarized beam is transmitted through the P1 polarizer and is directed towards beam dump BD1.

Harmonic separator S1 is used to separate the p-polarized second harmonic (SH) beam generated in the LBO1 crystal from the s-polarized unconverted fundamental beam. The separator is highly reflective for the SH beam and highly transmissive for the fundamental beam. The unconverted fundamental beam, separated from the SH by separator S1, is directed towards beam dump BD2. After separation, the SH is directed to the output via harmonic separator S2, and the leakage from S2 is utilized for diagnostics of both the SH and the unconverted fundamental beam. The leakage through S2 is directed to energy meter EM2 (Ophir PE10-C) for measuring the energy of the SH pulses using reflection from separator S3. The beam size is reduced by a telescope to fit to the EM2 aperture. In addition, the leakage through S3 is directed onto camera C2 through a demagnifying Keplerian telescope to capture the near-field profile of the SH beam reflected by separator S4. Finally, the leakage through S4 is directed via mirror M4 to camera C3 through a demagnifying telescope to capture the near-field profile of the unconverted fundamental beam. The demagnifying telescopes image the crystal position onto the cameras. Appropriate spectral filters are used in front of the energy meters and cameras to transmit only the harmonic to be observed. Similar to EM1 and C1, a PBS cube was placed before C2 and C3 to ensure that the p-polarized beam is directed to C2 and the s-polarized beam to C3, although it is omitted from [Figure 1](#) for simplicity. This approach helps mitigate potential effects caused by the polarization-dependent reflectivity and transmissivity of the optical elements in the diagnostic section of the setup.

Harmonic separator S1 and the LBO2 crystal for THG are mounted on a common motorized translation stage. This setup enables automated switching between the SH and third harmonic (TH) beams, making it well-suited for practical applications, for example when a wavelength dependence of the interaction is to be studied. When only the SH beam is required at the output, S1 is positioned in the beam path. Conversely, LBO2 is placed in the beam path when TH is required. The TH beam generated in the LBO2 crystal is separated from the SH and the remaining unconverted fundamental beam using harmonic separator S5, which is highly reflective for the TH beam and highly transmissive for the

fundamental and SH beams. The unconverted fundamental and SH beams separated from the TH beam are directed towards beam dump BD2. The generated TH is s-polarized; therefore, a half-wave plate HWP2 is used to convert its polarization to p-polarization in front of separator S6. After separation, the TH is directed to the output by reflection off S6. The leakage through S6 is reflected by S7 and directed to energy meter EM3 (Gentec QE12LP-H-MB-QED-D0) for measuring the energy of the TH pulses. The beam size is reduced by a telescope to match the EM3 aperture. In addition, the beam reflected by S8 is directed through a beam size reducing Keplerian telescope to camera C3 to capture the near-field profile of the TH beam. Appropriate band pass filters are placed in front of energy meter EM3 and camera C4 to filter out unwanted frequencies. The energy meters were calibrated in a way that the additional energy meters were placed into the output beams except EM1, measuring the fundamental beam, where the energy meter was placed in front of HWP1.

The LBO1 crystal (Raicol Crystals Ltd) used for SHG has an aperture of 30 mm × 30 mm and a length of 20 mm. The crystal is cut at angles  $\theta = 90^\circ$  and  $\phi = 11.6^\circ$  for type I ( $o + o \rightarrow e$ ) SHG in the XY plane. Both faces of the crystal are coated with dual-band anti-reflection (DBAR) coatings for 1064 and 532 nm. Similarly, the LBO2 crystal (Raicol Crystals Ltd) used for THG also has an aperture of 30 mm × 30 mm and a length of 20 mm. This crystal is cut at angles  $\theta = 42.4^\circ$  and  $\phi = 90^\circ$  for type II ( $o + e \rightarrow o$ ) THG in the YZ plane. The input face of the crystal is coated with DBAR coating for 1064 and 532 nm. The output face of the crystal has an anti-reflection coating for 355 nm. Note that although the crystals were cut for harmonic generation of a neodymium-doped yttrium aluminum garnet (Nd:YAG) laser, that is, 1064 nm fundamental wavelength, they were usable for the Yb:YAG-based laser system with a fundamental wavelength of 1030 nm as well. Both crystals are mounted in temperature-controlled ovens designed by the Faculty of Nuclear Sciences and Physical Engineering at the Czech Technical University in Prague, Czech Republic. These ovens have a temperature tuning range of 20°C–55°C with long-term stability better than  $\pm 0.01^\circ\text{C}$ .

### 3. Experimental results and discussion

#### 3.1. SHG experiments

The first set of experiments was focused on SHG. The laser operated at a repetition rate of 10 Hz, delivering pulses with a width of 8 ns and a Gaussian temporal profile. The energy incident on the crystal was slightly over 7 J. [Figure 2\(a\)](#) shows the spatial profile of energy fluence of the input beam at energy of 7 J. The cross-section near the beam center, extracted at specific X and Y coordinates, is indicated in [Figure 2\(a\)](#), including 10th-order super-Gaussian curve fits,

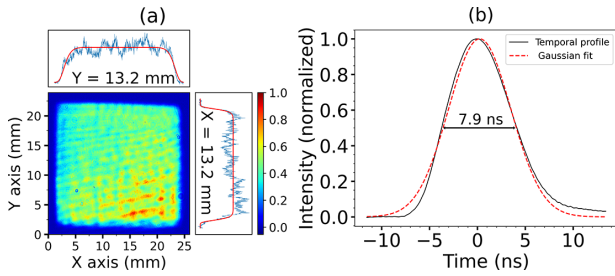


**Figure 2.** (a) Near-field profile of the input fundamental beam at 7 J. (b) Temporal profile of the fundamental beam.

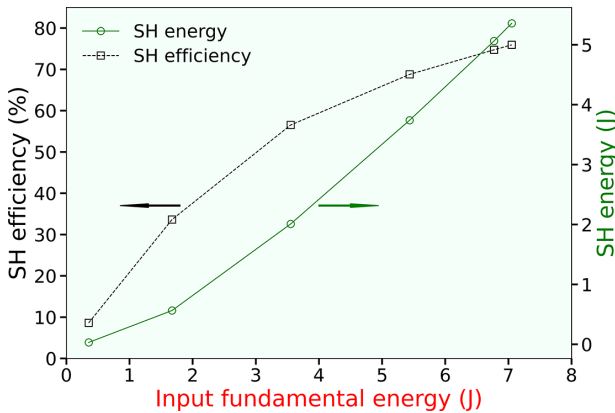
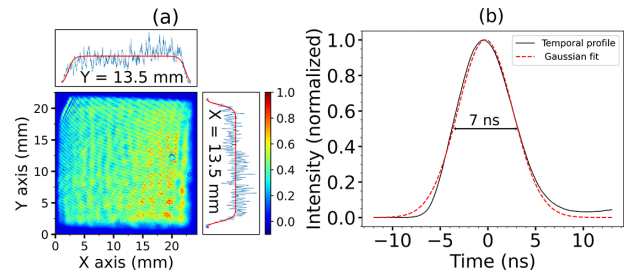


**Figure 3.** Dependence of the SH pulse energy on the input fundamental pulse energy, and the SHG conversion efficiency.

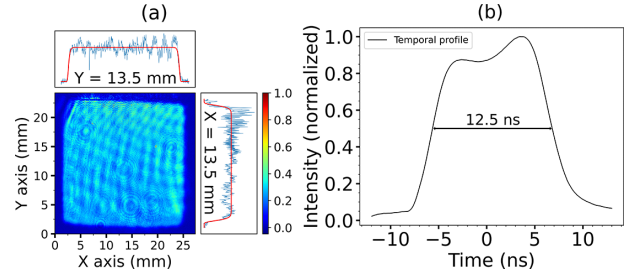
which are shown adjacent to it. Note that the beam from the laser is imaged onto the crystal and the near-field camera is in such position that it acquires an image corresponding to the crystal position. The beam size on the crystal is roughly  $22.1 \text{ mm} \times 20.2 \text{ mm}$  at full width at half maximum (FWHM). Figure 2(b) presents the temporal profile, with a measured width of 7.9 ns at FWHM. The pointing stability of the laser was also characterized over a 10-min period. The angular jitter, given as the standard deviation, was measured to be  $10 \text{ } \mu\text{rad}$  in the X direction and  $14 \text{ } \mu\text{rad}$  in the Y direction, demonstrating good beam pointing stability during the experiment. The LBO crystal was maintained at  $35^\circ\text{C}$ , and the pulse energy directed to the crystal was gradually increased up to 7.1 J using the attenuator during the experiment.

Figure 3 presents the SH pulse energy dependence and the corresponding SH conversion efficiency. As the fundamental energy increased, the SH energy rose accordingly, reaching a maximum of 5.3 J for a fundamental energy of 7.1 J, corresponding to a conversion efficiency of 75%. This represents a record conversion efficiency for a 10-J-class laser system utilizing Gaussian temporal profiles, surpassing the previously reported maximum SHG efficiency of 71.5%<sup>[19]</sup>.

Figures 4(a) and 5(a) depict the near-field energy fluence spatial profiles of the SH and unconverted fundamental beams, respectively. Similarly, Figures 4(b) and 5(b)



**Figure 4.** (a) Near-field profile of the SH beam at 5 J. (b) Temporal profile of the SH beam.



**Figure 5.** (a) Near-field profile of the unconverted fundamental beam. (b) Temporal profile of the unconverted fundamental beam.

illustrate the temporal profiles of the SH and unconverted fundamental pulses, respectively. The measured pulse width of the SH is 7 ns (FWHM), that is, about 1 ns shorter than the fundamental pulse due to the lower conversion efficiency at the lower intensities at the edges of the pulse. The unconverted pulse at the fundamental wavelength has a width of 12.5 ns, broadened due to pulse depletion around its peak. Note that the asymmetric profile is an artifact of the photodiode's temporal response. Comparing Figures 2(a) and 4(a) reveals the similarity in the near-field profile, indicating that higher intensity areas in the fundamental profile correspond to higher intensity areas in the SH profile.

We recorded the long-term pulse energy stability of the SH with its pulse energy exceeding 5 J for a little over 1 h and 15 min, as shown in Figure 6. To smooth out fluctuations and highlight longer trends, a floating average of 100 pulses is also shown in the figure. The measured SHG output pulse energy stability was 1.3% root mean square (RMS) (pulse-to-pulse), compared to 0.7% RMS (pulse-to-pulse) for the fundamental pulse measured over the same period. The stability of the conversion efficiency was measured as 0.96% RMS (pulse-to-pulse). While the trend of the SHG output pulse energy appears to follow that of the fundamental pulse, the conversion efficiency does not follow the same trend. This discrepancy arises because the SH efficiency starts to be saturated at the given fundamental energy, as indicated in the energy dependence graph in Figure 3. Consequently, changes in the fundamental and SH pulse energies do not significantly affect the conversion efficiency. However, a decrease in SH energy and conversion efficiency, along with a decrease in fundamental energy, is observed over time

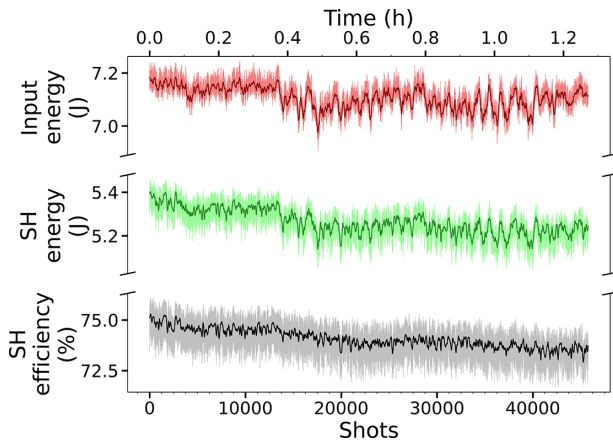


**Figure 6.** Long-term energy stability of the SH pulse energy. Light colored narrow lines show pulse-to-pulse energies, whereas the darker thick lines show the floating average over 100 pulses.

in the figure. The small long-term decrease by 1% of the fundamental pulse energy results in less than 2% long-term decrease of the SH pulse energy. The long-term decrease in SH energy is largely attributed to a reduction in the fundamental laser energy, accounting for approximately two-thirds of the SH drop. The remaining decline may be caused by thermal effects on optical components or by thermal gradients in the nonlinear crystal, although the exact source could not be determined from the experiments.

We measured the dependence of the SH pulse energy on the rotation of the LBO crystal about the vertical axis. The fundamental energy entering the crystal was set to 6.7 J, and the SH energy was measured while varying the angle ( $\phi$ ), that is, the angle between the wave vector of the fundamental beam, being in the XY plane of the LBO crystal, and the crystal's X-axis. To support the experimental results, simulations were performed using mLSNLO software from AS-Photonics<sup>[24]</sup>, specifically the 2D-mix-LP module, that is, the module that considers spatial profiles of the beam and long (ns) pulses. The simulation methodology follows the modeling approach outlined in Refs. [25,26], wherein the nonlinear Maxwell equations were solved using split-step Fourier methods. The inputs for simulations stemmed from the experiment. The experimental angular changes are related to angles outside the crystal. For comparison with calculated data the experimental angular changes were recalculated into internal angular changes. The refractive index of LBO crystal for the fundamental wavelength in the XY plane was calculated using the Sellmeier equation. Subsequently, the internal angles were determined by applying Snell's law. As shown in Figure 7, the internal angular acceptance bandwidths of the SHG in the LBO crystal were approximately 1.33 mrad ( $\sim 2.66$  mrad·cm) and 1.31 mrad ( $\sim 2.62$  mrad·cm) at FWHM for the experimental and simulation data, respectively. Hence, the experimental and simulated angular acceptance bandwidths are in good

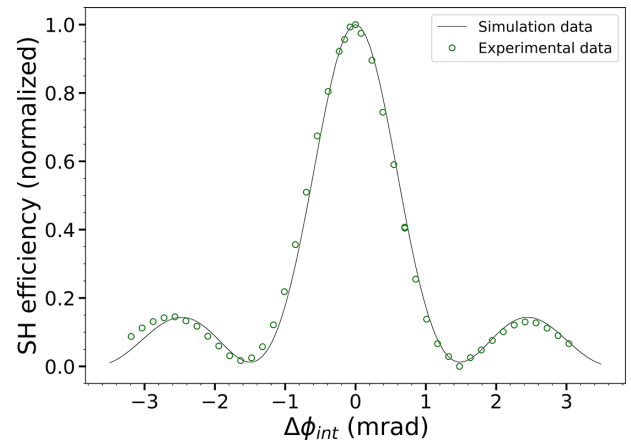


**Figure 7.** Dependence of the SH conversion efficiency on internal angular detuning for a 20 mm long LBO crystal.

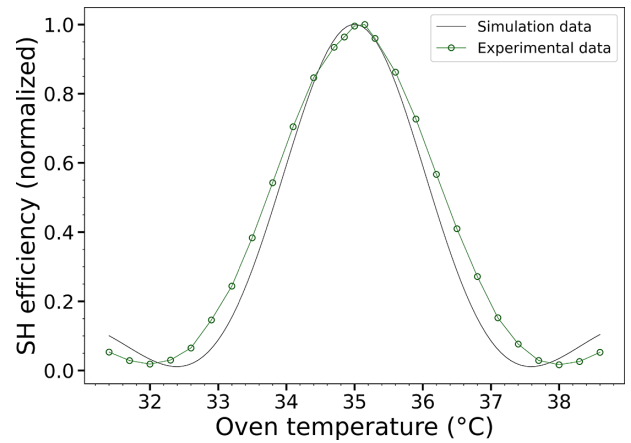


**Figure 8.** Dependence of the SH conversion efficiency on the oven temperature for a 20 mm long LBO crystal.

agreement. Also, the width of the calculated curve at 99% efficiency is 0.11 mrad, which approximately corresponds to an angular rotation of the crystal by 0.18 mrad. This implies that the external beam pointing fluctuation should be below  $\pm 0.09$  mrad to ensure that the SH conversion efficiency does not decrease by more than 1%.

To evaluate the sensitivity of SHG to temperature variations in the LBO crystal, we measured dependence of the SH pulse energy on the LBO crystal temperature. With the fundamental energy maintained at 6.5 J, we recorded the SH pulse energy at various oven temperatures. After each oven temperature change there was enough time for crystal thermalization. To complement our experimental findings, we performed simulations using the 2D-mix-LP module of the mLSNLO software for a more comprehensive analysis. As determined from Figure 8, the FWHM temperature acceptance bandwidths for the SHG in the LBO crystal were approximately 2.61 K ( $\sim 5.22$  K·cm) based on the experimental data and 2.3 K ( $\sim 4.6$  K·cm) according to the simulation data. The experimental and simulated results remain in

good agreement. The calculated temperature tolerance curve exhibits a width of 0.22 K at 99% efficiency. Therefore, the oven used for stabilizing the temperature of the LBO crystal during SHG should keep the crystal's temperature changes within  $\pm 0.11$  K to maintain stable conversion efficiency.

### 3.2. THG experiments

The next set of experiments focused on THG, achieved through sum frequency generation (SFG) between the SH and the unconverted fundamental beams. For these experiments, the fundamental energy was set to 6.1 J, which is lower than the energy used for SHG. This reduction corresponds to the smaller beam dimensions of 19.4 mm  $\times$  18.8 mm compared to those in the SHG experiments, and ensures operation at fluence levels matching those used in the SHG experiments. The beam size reduction utilizing a spatial light modulator<sup>[27]</sup> was done because the crystal used for THG was optimized for input fundamental wavelengths of 1064 nm, whereas the experiment utilized 1030 nm. Consequently, the crystal was rotated by approximately 12° about the vertical axis to change the  $\theta$  angle, that is, the angle between the crystal's Z-axis and the wave vector of the input beams in the YZ plane, which reduced its effective aperture, making beam reduction necessary. The spatial profile of the output at 6.1 J, and its cross-sections near the beam centers fitted with a 10th-order super-Gaussian profile, are shown in Figure 9. The oven temperature for both SHG and THG crystals was maintained at 35°C. After optimizing the angles of both the THG and SHG crystals, we achieved an output of 3.5 J at 343 nm with an efficiency of 56%. The SHG crystal required optimization to ensure that the conversion efficiency was not excessively high, as this would deplete the fundamental beam energy available for subsequent THG. In addition, the tilt of the THG crystal was carefully optimized to maximize the conversion efficiency for the SFG process. The dependence of THG energy and THG conversion efficiency is illustrated in Figure 10. Optimization of both the SHG and THG crystals was performed at the maximum available fundamental energy to ensure the best possible phase-matching conditions. Once optimized, the crystal tilts were kept constant during the subsequent energy dependence measurements to maintain consistency. To maximize conversion efficiency, the mixing ratio of the SH to the fundamental pulse energy was set to about 2:1.5, even though the theoretical optimum photon ratio is 2:1. This adjustment was necessary, because after the SHG process, the depleted fundamental output pulse is longer<sup>[28]</sup> and its temporal profile transitioned from a Gaussian to a double-Gaussian distribution, as shown in Figure 5(b). As a result, the temporal correlation between the fundamental and SH pulses is not ideal. To compensate for this mismatch, an imbalance in the mixing ratio was introduced. It is important to note that the ratio between the

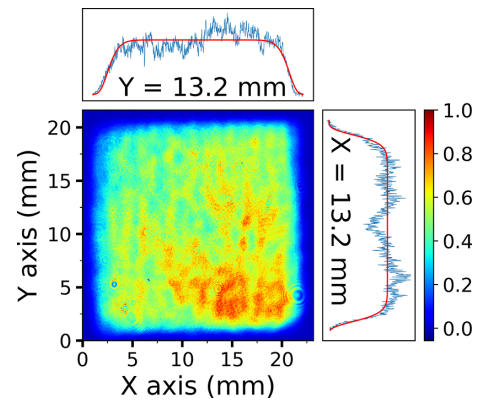


Figure 9. Near-field profile of the input fundamental beam at 6.1 J.

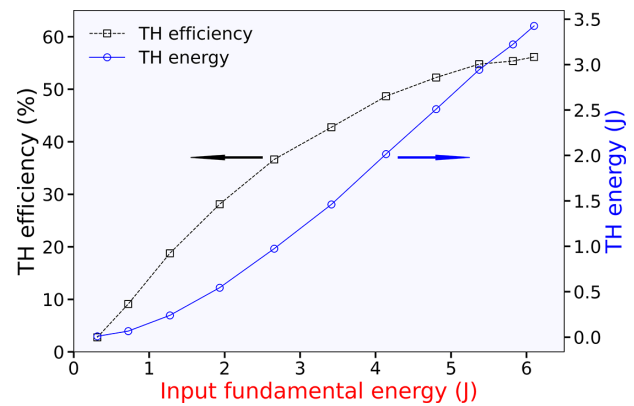


Figure 10. Dependence of the TH pulse energy on the input fundamental pulse energy, and the THG conversion efficiency.

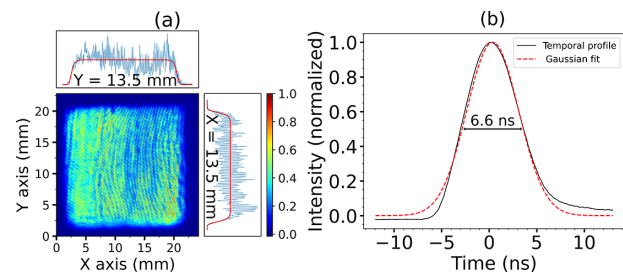
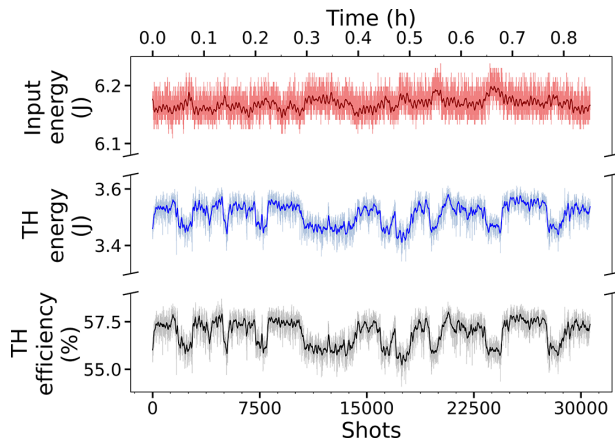


Figure 11. (a) Near-field profile of the TH beam at 3.5 J. (b) Temporal profile of the TH beam.

SH and the fundamental pulses was experimentally tuned to maximize the TH output. The optimal energy balance was determined through iterative adjustments during the experiment, specifically by tuning the LBO1 crystal tilt to control the SH conversion efficiency. Figure 11(a) shows the near-field spatial distribution of the TH beam, while Figure 11(b) depicts the temporal profile of the TH pulse. The measured pulse width of the TH is 6.6 ns (FWHM).

We monitored the THG output energy over more than 30,000 shots (spanning 50 min) at a fundamental energy of 6.1 J, as depicted in Figure 12. To emphasize longer-term trends, a floating average of 100 pulses is also presented in the figure. The measured stability of the THG output energy



**Figure 12.** Long-term stability of the TH pulse energy. Light colored narrow lines show pulse-to-pulse energies, whereas the darker thick lines show the floating average over 100 pulses.

was 1.24% RMS (pulse-to-pulse), compared to 0.26% RMS (pulse-to-pulse) for the fundamental energy measured over the same period. The stability of the conversion efficiency was measured as 1.29% RMS (pulse-to-pulse). Both the TH pulse energy and efficiency trends appear to follow a similar pattern, although they do not seem to align with the trend of the input fundamental energy. However, upon closer examination, an inverse relationship can be partially observed. This discrepancy may be partly due to an increase in SHG as the fundamental energy rises, leading to an imbalance in the mixing ratio of the SH and unconverted fundamental energy for THG. The excess of the SH and the reduction in the fundamental component lead to the decrease in TH output.

The angular acceptance of the THG was determined in a similar way to SHG by measuring the output pulse energy as a function of the phase-matching angle of the THG crystal. The fundamental pulse energy input into the crystal was set to 4.7 J, and the TH pulse energy was measured while varying the angle ( $\theta$ ). The results are presented in Figure 13, alongside the simulation results obtained using the 2D-mix-LP module of the mISNLO software. Note that the angular changes are considered inside the crystal. The angular acceptance bandwidths for the THG in the LBO crystal were found to be 1.19 mrad ( $\sim 2.38$  mrad-cm) at FWHM for the experimental data and 1.29 mrad ( $\sim 2.58$  mrad-cm) for the simulation data, demonstrating a good agreement between the two. In addition, the width of the calculated curve at 99% efficiency is 0.07 mrad, which roughly translates to an angular crystal rotation of 0.11 mrad. This suggests that to maintain the TH conversion efficiency within a 1% variation, the external beam pointing fluctuation must remain below  $\pm 0.055$  mrad.

Lastly, the THG process at 343 nm was investigated over a temperature range of 33°C–37°C to determine the temperature acceptance bandwidth. With the fundamental

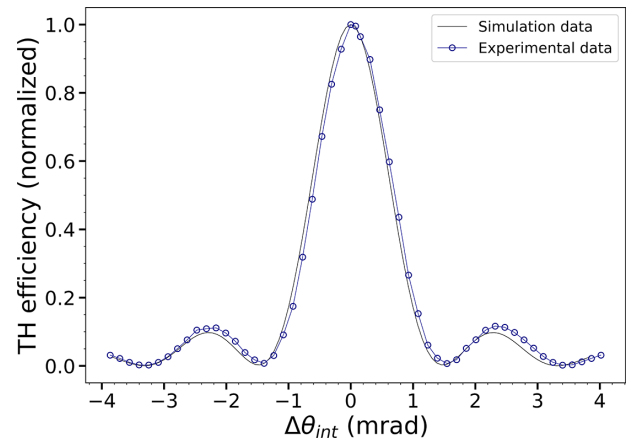


**Figure 13.** Dependence of the TH conversion efficiency on internal angular detuning for a 20 mm long LBO crystal.

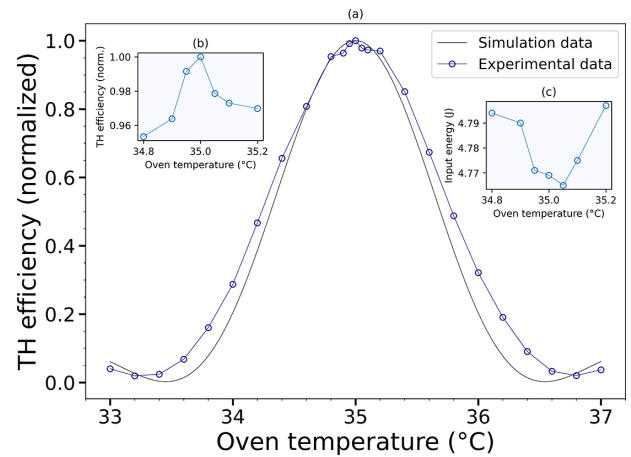


**Figure 14.** (a) Dependence of the TH conversion efficiency on the oven temperature for a 20 mm long LBO crystal. (b) Dependence of the TH conversion efficiency on the oven temperature with a reduced range of temperature points on the X-axis. (c) Input fundamental energy measured at different oven temperatures as it enters the crystal.

energy kept constant at 4.7 J, we measured the resulting TH pulse energy. In addition, simulations were conducted using the 2D-mix-LP module of mISNLO to provide a more detailed analysis. As shown in Figure 14(a), the temperature acceptance bandwidths for THG in the LBO crystal were approximately 1.35 K ( $\sim 2.70$  K-cm) based on experimental data and 1.55 K ( $\sim 3.1$  K-cm) according to simulation results, both measured at FWHM. The experimental and simulated results are in good agreement. Also, the inconsistency observed at the peak of the curve can be explained by examining Figures 14(b) and 14(c). A comparison between Figures 14(b) and 14(c) reveals that as the input fundamental energy decreases, the conversion efficiency increases. However, this trend is not strictly proportional, likely due to fluctuations in beam pointing and other instabilities that ultimately cause the peak of the curve to appear irregular. Furthermore, the calculated temperature tolerance curve has a width of 0.19 K at 99%

efficiency. Thus, to ensure optimal conversion efficiency during THG, the oven used for stabilizing the LBO crystal's temperature must maintain its temperature within  $\pm 0.095$  K or better.

#### 4. Conclusion

In this study, we explored the processes of SHG and THG using LBO crystals under controlled experimental conditions. For SHG, we achieved a peak conversion efficiency of 75%, yielding an output of 5.3 J at 515 nm. The output energy of SHG demonstrated a stability of 1.3% RMS, with a conversion efficiency stability of 0.96% RMS, for the fundamental energy stability of 0.7% RMS. The measured angular and temperature acceptance bandwidths for SHG closely matched the simulations.

In the case of THG, we obtained an output of 3.5 J at 343 nm, with a conversion efficiency of 56%. The THG process was notably sensitive to the mixing ratio of the SH and residual fundamental pulses. The output energy stability for THG was measured at 1.24% RMS, with a conversion efficiency stability of 1.29% RMS, for the fundamental energy stability of 0.26% RMS. The angular and temperature acceptance bandwidths for THG were consistent with the simulated predictions, although there is a small discrepancy in temperature acceptance bandwidth.

Overall, the results confirm the efficacy of LBO crystals for SHG and THG for high-energy high-power lasers, with most findings aligning well with theoretical models. Furthermore, the conversion efficiency could be increased by using a super-Gaussian temporal profile. In addition, the angular acceptance bandwidths for SHG and THG at FWHM exceed 2 mrad·cm, while the temperature acceptance bandwidth at FWHM surpasses 2.5 K·cm, both of which are notably large. We also demonstrate the long-term stability of these processes in LBO crystals, affirming the robustness of the frequency conversion. These findings collectively highlight LBO as an excellent crystal choice for efficient harmonic generation in high-energy, high-average-power laser applications. An important advantage demonstrated in this work is the ability to automatically switch between SHG and THG outputs without requiring physical realignment of the setup. This flexibility greatly enhances operational convenience and makes the system particularly attractive for applications requiring rapid switching between harmonics. In addition, we have developed a versatile system that can be easily adapted with only minor adjustments to accommodate both Nd:YAG and Yb:YAG lasers, thereby broadening its applicability across diverse laser platforms.

#### Acknowledgements

This work was supported by the Technology Agency of the Czech Republic (TM03000045). This work was

co-funded by the European Union and the state budget of the Czech Republic under the project LasApp (CZ.02.01.01/00/22\_008/0004573).

#### References

1. T. Tajima and J. M. Dawson, *Phys. Rev. Lett.* **43**, 267 (1979).
2. H. Y. Al-Omari, M. E. Yahia, and A. M. Almomani, *Phys. Rev. Accel. Beams* **27**, 073501 (2024).
3. U. Klotzbach, A. F. Lasagni, M. Panzner, and V. Franke, *Laser Micromachining* (Springer Berlin Heidelberg, Berlin, Heidelberg, 2011), pages 29–46.
4. J. Kaufman, D. Bricín, Z. Špirit, J. Strejcius, J. Šmaus, S. Pathak, Z. Fulín, J. Brajer, and T. Mocek, *Eng. Failure Anal.* **167**, 108982 (2025).
5. O. Stránský, L. Beránek, S. Pathak, J. Šmaus, J. Kopeček, J. Kaufman, M. Böhm, J. Brajer, T. Mocek, and F. Holešovský, *Virtual Phys. Prototyp.* **19**, e2340656 (2024).
6. H. Hora, J. Badziak, M. N. Read, Y.-T. Li, T.-J. Liang, Y. Cang, H. Liu, Z.-M. Sheng, J. Zhang, F. Osman, G. H. Miley, W. Zhang, X. He, H. Peng, S. Glowacz, S. Jablonski, J. Wolowski, Z. Skladanowski, K. Jungwirth, K. Rohlena, and J. Ullschmied, *Phys. Plasmas* **14**, 072701 (2007).
7. J. M. Di Nicola, T. Suratwala, L. Pelz, J. Heebner, R. Aden, D. Alessi, S. Amula, A. Barnes, A. Bhasker, T. Bond, J. Bude, B. Buckley, D. Browning, J. Cabral, A. CalónicoSoto, W. Carr, L. Chang, J. Chou, S. Cohen, T. Cope, D. Cross, R. Deveno, P. DeVore, A. Deland, P. Di Nicola, T. Dumbacher, G. Erbert, M. Erickson, A. Erlandson, C. Filip, D. Fratanduono, N. Gottesman, A. Gowda, A. Handler, V.J. Hernandez, S. Herriot, J. Horner, R. House, D. Kalantar, L. Kegelmeyer, C. Kinsella, T. Lanier, D. Larson, B. Le Galloudec, J. Lusk, B. MacGowan, S. McLaren, K. Manes, K. McCandless, G. Mennerat, C. Miller, M. Monticelli, R. Muir, R. Negres, J. Nelson, M. Nostrand, M. Ordoñez, C. Orth, E. Padilla, A. Pao, J. Penner, T. Petersen, M. Prantil, R. Raman, S. Rana, B. Raymond, N. Ruiz, R. Sacks, S. Schrauth, M. Shaw, S. Sommer, L. Siegel, M. Spaeth, C. Stolz, M.F. Tam, T. Tate, S. Trummer, D. VanBlarcom, K. Varadan, A. Vella, A. Wargo, L. Wang, L. Waxer, P. Wegner, B. Welday, P. Whitman, C. Widmayer, W. Williams, L. Wong, N. Wong, B. Van Wouterghem, S. Yang, and G. Brunton, *High Energy Density Phys.* **52**, 101130 (2024).
8. H. Abu-Shawareb, *et al.*, *Phys. Rev. Lett.* **132**, 065102 (2024).
9. R. Paschotta, Ytterbium-doped laser gain media, [https://www.rp-photonics.com/ytterbium\\_doped\\_laser\\_gain\\_media.html](https://www.rp-photonics.com/ytterbium_doped_laser_gain_media.html) (2025).
10. W. F. Krupke, *IEEE J. Select. Top. Quantum Electron.* **6**, 1287 (2000).
11. M. Divoký, J. Pilař, M. Hanuš, P. Navrátil, O. Denk, P. Severová, P. Mason, T. Butcher, S. Banerjee, M. De Vido, C. Edwards, J. Collier, M. Smrž, and T. Mocek, *Opt. Lett.* **46**, 5771 (2021).
12. C. Wandt, S. Klingebiel, S. Keppler, M. Hornung, M. Loeser, M. Siebold, C. Skrobol, A. Kessel, S. A. Trushin, Z. Major, J. Hein, M. C. Kaluza, F. Krausz, and S. Karsch, *Laser Photonics Rev.* **8**, 875 (2014).
13. A. Lyachev, I. O. Musgrave, Y. Tang, C. Hernandez-Gomez, I. N. Ross, M. Galimberti, O. V. Chekhlov, and J. Collier, *Opt. Express* **19**, 15824 (2011).
14. D. N. Papadopoulos, J. P. Zou, C. Le Blanc, G. Chériaux, P. Georges, F. Druon, G. Mennerat, P. Ramirez, L. Martin, A. Fréneaux, A. Beluze, N. Lebas, P. Monot, F. Mathieu, and P. Audebert, *High Power Laser Sci. Eng.* **4**, e34 (2016).
15. A. Bayramian, J. Armstrong, G. Beer, R. Campbell, B. Chai, R. Cross, A. Erlandson, Y. Fei, B. Freitas, R. Kent, J. Menapace, W. Molander, K. Schaffers, C. Siders, S. Sutton, J. Tassano, S.

- Telford, C. Ebberts, J. Caird, and C. Barty, *J. Opt. Soc. Am. B* **25**, B57 (2008).
16. S. Y. Park, Y. Choi, Y. H. Seo, H. Kim, D. H. Lee, P. L. Truong, Y. Jeon, H. Yoo, S. J. Kwon, D. Lee, and E.-S. Cho, *Micromachines* **15**, 103 (2024).
  17. J. P. Phillips, S. Banerjee, J. Smith, M. Fitton, T. Davenne, K. Ertel, P. Mason, T. Butcher, M. De Vido, J. Greenhalgh, C. Edwards, C. Hernandez-Gomez, and J. Collier, *Opt. Express* **24**, 19682 (2016).
  18. J. P. Phillips, S. Banerjee, P. Mason, J. Smith, J. Spear, M. De Vido, K. Ertel, T. Butcher, G. Quinn, D. Clarke, C. Edwards, C. Hernandez-Gomez, and J. Collier, *Opt. Lett.* **46**, 1808 (2021).
  19. T. Sekine, H. Sakai, Y. Takeuchi, Y. Hatano, T. Kawashima, H. Kan, J. Kawanaka, N. Miyanaga, and T. Norimatsu, *Opt. Express* **21**, 8393 (2013).
  20. H. Chi, Y. Wang, A. Davenport, C. S. Menoni, and J. J. Rocca, *Opt. Lett.* **45**, 6803 (2020).
  21. M. Divoky, J. Phillips, J. Pilar, M. Hanus, P. Navratil, O. Denk, T. Paliesek, P. Severova, D. Clarke, M. Smrz, T. Butcher, C. Edwards, J. Collier, and T. Mocek, *High Power Laser Sci. Eng.* **11**, e65 (2023).
  22. J. Pilar, M. Divoky, J. Phillips, M. Hanus, P. Navratil, O. Denk, P. Severova, T. Paliesek, D. Clarke, M. Smrz, T. Butcher, C. Edwards, and T. Mocek, *High Power Laser Sci. Eng.* **12**, e96 (2024).
  23. P. Mason, M. Divoký, K. Ertel, J. Pilař, T. Butcher, M. Hanuš, S. Banerjee, J. Phillips, J. Smith, M. De Vido, A. Lucianetti, C. Hernandez-Gomez, C. Edwards, T. Mocek, and J. Collier, *Optica* **4**, 438 (2017).
  24. <https://as-photonics.com/products/mlsnlo/>.
  25. A. V. Smith and M. S. Bowers, *J. Opt. Soc. Am. B* **12**, 49 (1995).
  26. A. V. Smith, W. J. Alford, T. D. Raymond, and M. S. Bowers, *J. Opt. Soc. Am. B* **12**, 2253 (1995).
  27. T. Paliesek, P. Navrátil, J. Pilař, M. Divoký, M. Smrž, and T. Mocek, *High Power Laser Sci. Eng.* **11**, e79 (2023).
  28. R. Eckardt and J. Reintjes, *IEEE J. Quantum Electron.* **20**, 1178 (1984).